Tony L. Schmitz
e-mail: tony.schmitz@nist.gov,

Matthew A. Davies
e-mail: matthew.davies@nist.gov,

Michael D. Kennedy

Manufacturing Metrology Division,
National Institute of Standards and Technology,
100 Bureau Drive, MS 8220,
Gaithersburg, MD 20899

Tool Point Frequency Response Prediction for High-Speed Machining by RCSA

The implementation of high-speed machining for the manufacture of discrete parts requires accurate knowledge of the system dynamics. We describe the application of receptance coupling substructure analysis (RCSA) to the analytic prediction of the tool point dynamic response by combining frequency response measurements of individual components through appropriate connections. Experimental verification of the receptance coupling method for various tool geometries (e.g., diameter and length) and holders (HSK 63A collet and shrink fit) is given. Several experimental results are presented to demonstrate the practical applicability of the proposed method for chatter stability prediction in milling. [DOI: 10.1115/1.1392994]

1 Introduction

Recent improvements in machine and spindle designs have led to the increased use of high-speed machining (HSM) in the manufacture of discrete parts, especially in the aerospace industry [1]. It is recognized that a major practical limitation on the productivity of HSM systems is regenerative chatter. Therefore, many studies have explored methods to maximize material removal rate (MRR) during HSM, while avoiding chatter. This research has included the accurate measurement of machine dynamics, self-excited vibration theory for the calculation of stability lobes, machine/spindle design requirements, and sensors capable of chatter recognition, as well as the analytic and numerical time-domain simulation of the cutting forces and tool deflections during HSM [2–14]. HSM simulation, which is crucial for pre-process chatter prediction and avoidance, requires knowledge of the system dynamics reflected at the tool point. In general, a separate set of tool point frequency response function (FRF) measurements must be performed for each tool/holder/spindle combination on a particular machining center. These measurements can prove time-consuming, require a trained technician, and lead to costly machine downtime. In this work, we seek to reduce measurement time and increase process efficiency by predicting the tool point dynamic response using receptance coupling substructure analysis (RCSA) [15]. This method couples component frequency responses (e.g., tool, holder/spindle) through appropriate connections using simple vector manipulations and will be described in the following sections. Experimental verification of the method will be provided for: (1) a *tool tuning* example (i.e., adjusting tool length to make use of local increases in machining stability as shown in [4] and [16]) using 12.7 mm diameter endmills and a collet-type HSK 63A holder, (2) a 19.1 mm diameter endmill coupled to a shrink-fit HSK 63A holder (including mode shapes predictions), and (3) a *tool tuning* case study for 6.35 mm diameter endmill with collet holder.

1.1 High-Speed Machining. As the application of HSM in production environments grows, interest in rapid efficient methods for identifying stable cutting parameters also increases. Fundamentally, HSM seeks to increase chip width, and the corresponding MRR, by selecting a tooth passing frequency that is equal to the natural frequency (or any of its fractional harmonics) of the most flexible system mode [7]. A useful graphical tool for the selection of these spindle speeds is the well-known stability lobe diagram.

Stability lobe diagrams, which predict system stability as a function of selected machining parameters, are commonly used to select the best available spindle speed for maximized MRR. Stable and unstable regions (separated by the stability ''lobes'') are seen in these diagrams, depending on the selected spindle speed and axial depth of cut, b. Stability lobe diagrams may be calculated using analytic (see, for example, [8–11]) or numerical time-domain techniques [7]. In either instance, knowledge of the tool/workpiece/machine dynamics, specifically the tool point FRF, is required. In many cases, the system dynamics are obtained using impact testing and modal analysis. The direct FRF is measured at the tool point and multiple modes fit to the results. Modal parameters (i.e., mass, m, stiffness, k, and damping coefficient, c) for each of the selected modes are extracted and used as input to the stability lobe analysis [4,7–11,17,18]. Other possibilities include computational methods for modal parameter determination and milling experiments for direct stable speed selection. For the latter, modal parameters are not determined or required. Using stability lobe theory, machining tests are completed to locate chatter frequencies and select stable spindle speeds [18]. In all cases, however, the measurements are specific to the selected components (e.g., tool and tool length, holder, workpiece, spindle, and machine) and boundary conditions (e.g., holder force and drawbar force, as shown in [19]).

2 Receptance Coupling

In receptance coupling substructure analysis, experimental or analytic direct and cross FRFs for the individual components are used to predict the final assembly's dynamic response at any spatial coordinate selected for component measurements [20–23]. In this method, unlike modal coupling and finite element analyses, experimental or analytic FRFs are required only at the coordinate of interest (the tool point, in this case) and any connection coordinates; the number of modeled structural modes in each component does not define the number of required measurement locations (e.g., to obtain square modal matrices); and no matrix inversions are necessary (only vector manipulations are required). In the following sub-sections, descriptions of the RCSA method for two different physical models will be given.

2.1 RCSA Description I. The receptance matrix, $G(\omega)$, for the (contrived) assembled system shown in Fig. 1 will now be derived using the receptance coupling method [21]. The 2×2 receptance matrix (for the two degree-of-freedom system) will be

Contributed by the Manufacturing Engineering Division for publication in the JOURNAL OF MANUFACTURING SCIENCE AND ENGINEERING. Manuscript received September 2000; revised January 2001. Associate Editor: Y. Altintas.

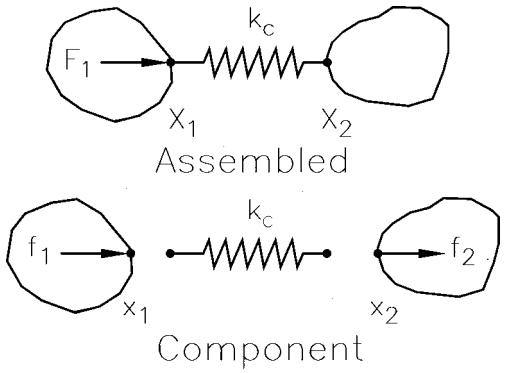

Fig. 1 RCSA Description I: assembled/component systems

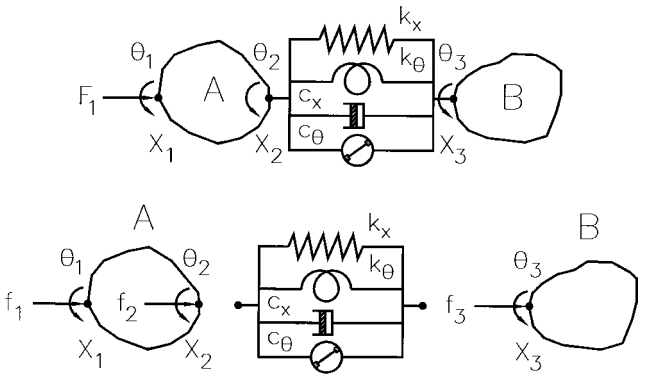

Fig. 2 RCSA Description II: tool/holder/spindle assembly model

calculated by columns. We will determine the first column by applying a virtual force, F_1, to the assembly coordinate X_1. Figure 1 displays both the assembled and component systems with F_1 applied to the assembled system.

Considering the (unassembled) substructures in Fig. 1, the displacements at the two coordinates can be written as shown in Eq. (1). The notation H refers to the spatial receptance matrices of the individual components before assembly. The equilibrium condition for the components is given in Eq. (2). The compatibility conditions are shown in Eq. (3).

$$\begin{aligned} x_1 &= H_{11} f_1 \\ x_2 &= H_{22} f_2 \end{aligned} \tag{1}$$

$$f_1 + f_2 = F_1, \quad \text{and} \quad f_1 = F_1 - f_2 \tag{2}$$

$$X_1 = x_1, \quad X_2 = x_2, \quad \text{and} \quad x_2 - x_1 = \frac{-f_2}{k_c} \tag{3}$$

Substitution of Eqs. (1) and (2) into (3) yields Eq. (4). Substituting the result shown in (4) into the equilibrium condition gives (5). These are expressions for the forces acting on the individual components.

$$f_2 = \left(H_{11} + H_{22} + \frac{1}{k_c} \right)^{-1} H_{11} F_1 \tag{4}$$

$$f_1 = \left(1 - \left(H_{11} + H_{22} + \frac{1}{k_c} \right)^{-1} H_{11} \right) F_1 \tag{5}$$

The first column of the receptance matrix is now determined by substitution into the appropriate displacement/force relationships. Equations (6) and (7) give expressions for the $G_{11}(\omega)$ and $G_{21}(\omega)$ receptance terms.

$$G_{11}(\omega) = \frac{X_1}{F_1} = H_{11} - H_{11} \left(H_{11} + H_{22} + \frac{1}{k_c} \right)^{-1} H_{11} \tag{6}$$

$$G_{21}(\omega) = \frac{X_2}{F_1} = H_{22} \left(H_{11} + H_{22} + \frac{1}{k_c} \right)^{-1} H_{11} \tag{7}$$

The second column of the receptance matrix is found by applying a virtual force, F_2, to coordinate X_2 of the assembly. The displacements for this case are the same as those given in Eq. (1). The new equilibrium and compatibility equations are shown in Eqs. (8) and (9), respectively. Substitution and combining operations similar to those for the first column give expressions for $G_{12}(\omega)$ and $G_{22}(\omega)$.

$$f_1 + f_2 = F_2, \quad \text{and} \quad f_2 = F_2 - f_1 \tag{8}$$

$$X_1 = x_1, \quad X_2 = x_2, \quad \text{and} \quad x_1 - x_2 = \frac{-f_1}{k_c} \tag{9}$$

$$G_{12}(\omega) = \frac{X_1}{F_2} = H_{11} \left(H_{11} + H_{22} + \frac{1}{k_c} \right)^{-1} H_{22} \tag{10}$$

$$G_{22}(\omega) = \frac{X_2}{F_2} = H_{22} - H_{22} \left(H_{11} + H_{22} + \frac{1}{k_c} \right)^{-1} H_{22} \tag{11}$$

2.2 RCSA Description II. A second example of receptance coupling will be described for the assembly shown in Fig. 2 and signifies the physical case of tool point FRF prediction. This model represents the connection of a tool (component *A*) to a particular holder/spindle combination (component *B*) by linear and torsional springs and dampers (which depend mainly on the contact conditions between the tool and holder). It is similar to the example in the previous section, except there are now three spatial coordinates of interest (with translation and rotation considered at each) and damping is included.

The RCSA derivation for the tool point direct FRF, $G_{11}(\omega)$, is analogous to the example in Section 2.1 (the other receptance matrix terms may also be determined, but only G_{11} is required for stability prediction). As shown previously, a virtual force, F_1, is applied to coordinate X_1 of the assembly (see Fig. 2). The displacements/rotations, equilibrium conditions, and compatibility conditions are then determined for this loading case, as shown in Eqs. (12)–(14), and are combined to calculate the assembly direct FRF at X_1. For this model, response functions that relate displacement to applied moment (L_{ij}), rotation to applied force (N_{ij}), and rotation to applied moment (P_{ij}) are also included. The result for G_{11} is shown in Eq. (15), where the H'_{ij}, L'_{ij}, N'_{ij}, and P'_{ij} terms represent mobility FRFs [24], or the ratio of linear or rotational velocity to force or moment (due to the velocity dependence introduced by viscous damping). The linear and rotational stiffness and damping terms are labeled k_x, k_θ, c_x, and c_θ, respectively.

$$\begin{aligned} x_1 &= H_{11} f_1 + H_{12} f_2 + L_{12} m_2 \\ x_2 &= H_{21} f_1 + H_{22} f_2 + L_{22} m_2 \\ x_3 &= H_{33} f_3 + L_{33} m_3 \\ \theta_1 &= N_{11} f_1 + N_{12} f_2 + P_{12} m_2 \\ \theta_2 &= N_{21} f_1 + N_{22} f_2 + P_{22} m_2 \\ \theta_3 &= N_{33} f_3 + P_{33} m_3 \end{aligned} \tag{12}$$

$$f_1 = F_1, \quad f_2 + f_3 = 0, \quad \text{and} \quad m_2 + m_3 = 0 \tag{13}$$

$$X_i = x_i, \quad \Theta_i = \theta_i, \quad k_x(x_3 - x_2) + c_x(\dot{x}_3 - \dot{x}_2) = -f_3,$$

and

$$k_\theta(\theta_3 - \theta_2) + c_\theta(\dot{\theta}_3 - \dot{\theta}_2) = -m_3 \tag{14}$$

$$G_{11}=H_{11}-H_{12}E_1^{-1}E_2-L_{12}E_3^{-1}((k_\theta N_{21}+c_\theta N'_{21})-E_4E_1^{-1}E_2) \tag{15}$$

where,

$$E_1=(k_xH_{33}+k_xH_{22}+c_xH'_{33}+c_xH'_{22}+[1])$$
$$-E_3^{-1}E_4(k_xL_{33}+k_xL_{22}+c_xL'_{33}+c_xL'_{22})$$
$$E_2=(k_xH_{21}+c_xH'_{21})-E_3^{-1}(k_\theta N_{21}+c_\theta N'_{21})$$
$$(k_xL_{33}+k_xL_{22}+c_xL'_{33}+c_xL'_{22})$$
$$E_3=(k_\theta P_{33}+k_\theta P_{22}+c_\theta P'_{33}+c_\theta P'_{22}+[1])$$
$$E_4=(k_\theta N_{33}+k_\theta N_{22}+c_\theta N'_{33}+c_\theta N'_{22})$$

3 Component Frequency Response Functions

Three primary steps are involved in the prediction of the tool point response for an assembled tool/holder/spindle system by RCSA: (1) define an appropriate model which includes all necessary degrees of freedom and connection terms, (2) determine the component FRFs by measurement or analytic/finite element prediction, and (3) couple the component FRFs through the modeled connections. In this section we describe the methods used to obtain the required component FRFs (i.e., tool and holder/spindle combination).

The component FRFs were determined in two distinct parts. First, the direct and cross free-free state (or unsupported) FRFs for coordinates x_1 and x_2 of component *A* (the tool) were calculated analytically. An analytical formulation, rather than experimental measurement, was selected due to the difficulties associated with obtaining these tool FRFs using impact testing (e.g., the free-free state is difficult to realize in practice; low mass, wide bandwidth accelerometers typically do not perform well at low frequencies and zero frequency, rigid body mode behavior may not be well represented in the measurements; and the response for low mass tools is easily corrupted by the accelerometer mass). A finite element solution is also a viable alternative. Second, the direct FRFs at coordinate x_3 of component B (the holder/spindle) were obtained experimentally using impact testing. *The combination of the analytic/finite element FRFs for the tool (which is simple to model) with the experimental direct FRF for the holder/spindle (which is difficult to model analytically) is a unique capability of the RCSA method and allows a direct evaluation of the effects of changes in tool parameters (e.g., length, diameter, density) on the assembly dynamics and process stability without repeated experimental measurements*.

A brief description of the analytic derivation of the tool FRFs will now be given. Figure 3 shows the loads applied to the tool when connected to the holder/spindle. A force is applied to the free end (x_1) while the end to be inserted in the holder (x_2) opposes displacement and rotation (i.e., a cantilever beam). The equation of motion for this model is shown in Eq. (16). Here, $u(x,t)$ is the temporal displacement at any point along the beam and $q(x,t)$ represents the externally applied loads. Additionally, ρ is the beam mass per unit length, c' is the viscous damping coefficient per unit length, E is Young's modulus (homogeneity assumed), and I is the second area moment of inertia.[1]

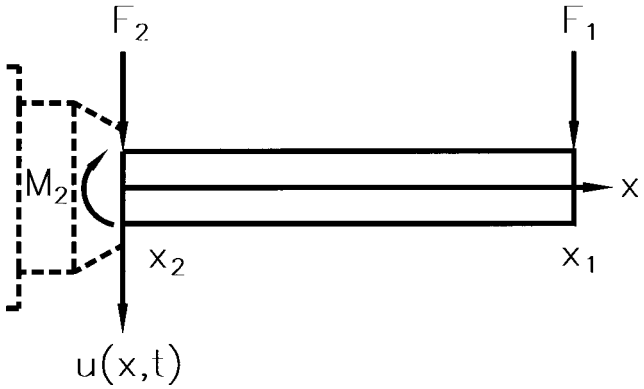

Fig. 3 Tool loading conditions

$$\rho\frac{\partial^2u(x,t)}{\partial t^2}+c'\frac{\partial u(x,t)}{\partial t}+EI\frac{\partial^4u(x,t)}{\partial x^4}=q(x,t) \tag{16}$$

If harmonic motion is assumed, a solution for the lateral vibration of the beam at any coordinate along its length (L) may be obtained from Eq. (16) for each beam mode. These results are then summed to determine the total vibration at that location.

In this analysis, two rigid body modes (inertial translation and rotation about the center of mass defined in Eq. (17), respectively) were combined with analytic expressions for the beam free-free modes [25] to approximate the tool vibration. These orthogonal modes were normalized according to Eq. (18). Expressions for the direct (complex displacement over force) FRFs at coordinates x_1 and x_2 (H_{11} and H_{22}, respectively) and a cross FRF H_{12} (H_{21} is equivalent by reciprocity) are shown in Eq. (19), where λ_i is a dimensionless frequency parameter (e.g., the first three free-free beam modes have corresponding λ values of 4.7300474, 7.85320462, and 10.9956079, respectively [25]).

$$\varphi_1(x)=1$$
$$\varphi_2(x)=\frac{\sqrt{12}}{L}\left(x-\frac{L}{2}\right) \tag{17}$$

$$\int_0^L\varphi_i(x)\cdot\varphi_j(x)dx=\begin{cases}0, & i\neq j\\ L, & i=j\end{cases} \tag{18}$$

The receptance term H_{11}, for example, contains three components. The first two represent the contributions by the translational and rotational rigid body modes, respectively, while the third gives the response due to the free-free modes $\phi_i(x)$, expressed as shown in Eq. (20), which have been evaluated at coordinate x_1 (a distance L from the model origin). Response functions that relate displacement to applied moment (L_{ij}), rotation to applied force (N_{ij}), and rotation to applied moment (P_{ij}) were also derived.

$$H_{11}(\omega)=\frac{1}{-\rho L\omega^2}+\frac{3}{-\rho L\omega^2}+\sum_{i=1}^{\infty}\frac{\varphi_i(L)^2}{-\rho L\omega^2+ic'L\omega+\frac{EI\lambda_i^4}{L^3}}$$

$$H_{22}(\omega)=\frac{1}{-\rho L\omega^2}+\frac{3}{-\rho L\omega^2}+\sum_{i=1}^{\infty}\frac{\varphi_i(0)^2}{-\rho L\omega^2+ic'L\omega+\frac{EI\lambda_i^4}{L^3}} \tag{19}$$

$$H_{12}(\omega)=\frac{1}{-\rho L\omega^2}-\frac{3}{-\rho L\omega^2}+\sum_{i=1}^{\infty}\frac{\varphi_i(L)\varphi_i(0)}{-\rho L\omega^2+ic'L\omega+\frac{EI\lambda_i^4}{L^3}}$$

$$\varphi_i(x)=\cosh\frac{\lambda_ix}{L}+\cos\frac{\lambda_ix}{L}-\sigma_i\left(\sinh\frac{\lambda_ix}{L}+\sin\frac{\lambda_ix}{L}\right) \tag{20}$$
$$\sigma_i=\frac{\cosh\lambda_i-\cos\lambda_i}{\sinh\lambda_i-\sin\lambda_i}$$

The validity of the analytic tool model was tested in simulation. The free-free beam model (consisting of direct and cross FRFs) was attached to ground through infinitely stiff linear and rotational

[1] A uniform cylindrical cross-section has been assumed due to the short flute lengths for the tooling used in this study. However, for long flute lengths it becomes necessary to consider the actual geometry of the twisted end mill.

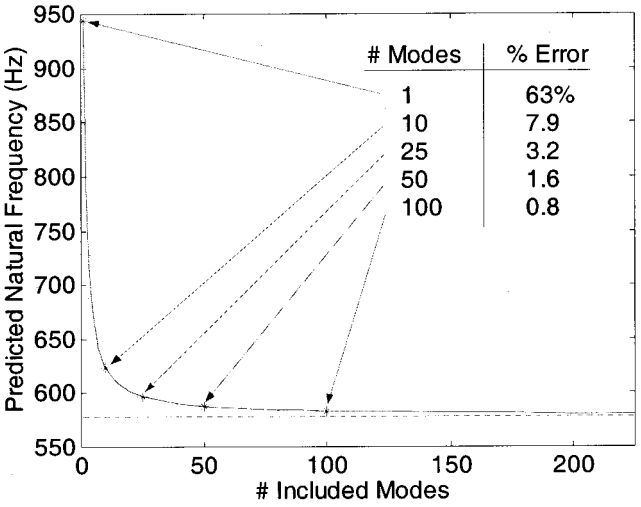

Fig. 4 Cantilever response convergence

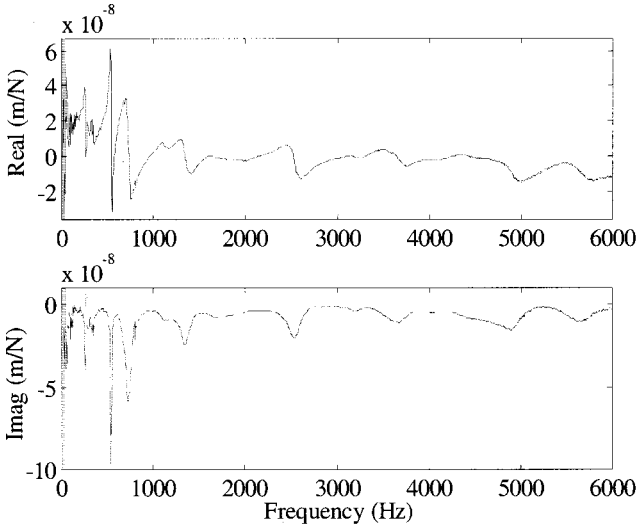

Fig. 5 Measured FRF of HSK 63A collet/spindle combination (Y-direction)

springs to verify that the assembly response at the free end approached that of a cantilever beam. It was determined that many free-free modes were necessary to adequately model the cantilever response. This problem has also been addressed in the use of the modal analysis technique referred to as Structural Dynamic Modification (SDM), an analytic tool that uses modal data to estimate variations in the dynamic response of a system due to changes in the mass, damping, and/or stiffness. In this method, it is recognized that the inability to measure/model all the system modes (i.e., modal truncation) leads to various levels of prediction inaccuracies depending on the nature of the structure. For example, Avitabile [26] evaluated the use of free-free beam modes (with appropriate boundary conditions applied) to approximate the behaviors of simply supported and cantilever beams. The results showed that the simply supported modes were well-characterized because they may be expressed as a linear combination of the free-free modes (e.g., the first simply supported mode is well-approximated by the sum of the translational rigid body and first bending modes for the free-free beam). This is not the case for the cantilever beam. The primary limitation here is that free-free modes do not exhibit curvature at the beam ends, while the cantilever model requires a large curvature at the clamped end to generate an accurate response.

In Fig. 4, the variation in the predicted natural frequency for a 19.1 mm diameter, 152.4 mm long aluminum shaft as a function of the number of included modes is shown. It is seen that approximately 86 modes are necessary to predict a value within 1 percent of the analytically predicted cantilever frequency of 578.6 Hz (shown as the dashed line in Fig. 4). This large number of required modes for accurate frequency prediction precludes the exclusive use of experimental techniques to obtain the free-free tool response (due to limited measurement bandwidth), but is well suited to analytic predictions.

For component B (the holder/spindle combination), only the direct FRFs at the connection coordinate (H_{33}, L_{33}, N_{33}, and P_{33}) are required. In this case, the direct FRF H_{33} was obtained by impact testing. A low mass, wide bandwidth accelerometer was placed at the free end of the collet HSK 63A holder and this location excited by a modally tuned impact hammer for both the X and Y coordinate directions. The remaining FRFs (pertaining to moment and rotation) were assumed zero (in the absence of reliable measurement techniques).

4 RCSA Verification Testing

To verify the receptance coupling technique, tests were carried out on three separate tool geometries and holders. First, three long, slender tools (length to diameter ratios of 8:1, 9:1, and 10:1) were selected for measurement in a 12.7 mm diameter collet holder (HSK 63A spindle connection). The tungsten carbide (cobalt binder) tools had two flutes and a relieved diameter of 11.8 mm for the entire portion of the tool outside the holder (12.7 mm inside). The length of the fluted portion was 15 mm. Second, a 19.1 mm diameter tungsten carbide endmill with two flutes and a 98.5 mm overhang (5.2:1 length to diameter ratio) was mounted in a shrink fit holder in the same spindle and the tool point response measured and predicted. Comparisons between predicted and measured mode shapes for this tool were also completed. Finally, the overhang length for a 6.35 mm diameter, 4 flute, tungsten carbide endmill (coupled to a collet-type HSK 63A holder) was selected for optimum MRR in a *tool tuning* case study.

4.1 11.8 mm Diameter Tooling. In order to predict the tool point response for a particular tool/holder/spindle assembly, three experimental measurements must be performed. First, as noted in Section 3, the holder/spindle direct FRFs (H_{33}) in the X and Y coordinate directions (mutually perpendicular to the spindle centerline) must be obtained. An example Y direction measurement for the collet holder/spindle combination to be coupled to the 8, 9, and 10:1 tools is shown in Fig. 5. Second, a single tool point direct FRF measurement must be completed (for a representative tool) and the connection coefficients (i.e., k_x, c_x, k_θ, and c_θ) selected to provide a match between the predicted and measured responses. These parameters are then used to predict the system responses for other configurations.

In this research, the following procedure was used to obtain the connection coefficients. First, the tool was secured in the spindle and the Y-direction tool point FRF was measured. The overhang was selected to be in the middle of the anticipated range (i.e., the 9:1 configuration with a 106.2 mm overhang). The connection parameters were then identified by displaying the predicted and measured FRFs in a single graph and varying the connection coefficients until a reasonable fit was obtained. The situation was simplified to a two variable problem by assuming the linear and rotational stiffnesses were proportional, as well as the linear and rotational damping terms. The fit then proceeded by adjusting a single stiffness multiplier to obtain a frequency match and a single damping multiplier for amplitude agreement. Although this was not a mathematically rigorous fitting procedure (it would be possible, for example, to pose the fit as a nonlinear optimization problem with an objective function that minimized the point-by-point difference between the two curves using four independent

Table 1 Stiffness/damping coefficients for 11.8 mm diameter, two flute tooling (identified from 9:1 configuration)

k_x (N/m)	k_θ (N-m/rad)	c_x(N-s/m)	c_θ (N-m-s/rad)
2.1×10^7	1.4×10^6	130	35

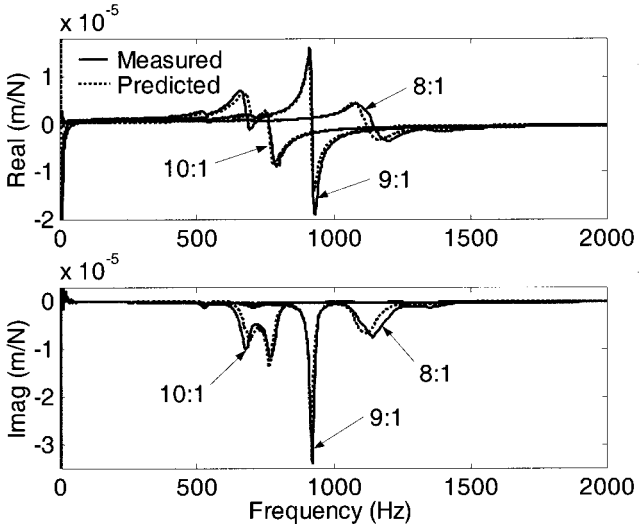

Fig. 6 Experimental/predicted Y direction tool point FRFs (8, 9, and 10:1 tools)

variables), it did provide a quick method for determining a set of connection coefficients with reasonable values based on physical intuition (i.e., they were not exceptionally high or low given engineering knowledge of the tool/tool holder interface). Obvious drawbacks to this technique include: (1) the requirement for a representative measurement of each tool/tool holder combination to be used, and (2) the need for dynamic consistency in the connection,[2] although it could be argued that the latter is a general requirement for the application of high-speed machining to shop floor production.

The selected linear and rotational spring and damping coefficients for the collet connection between the 11.8 mm tooling and holder/spindle are given in Table 1. It is anticipated that the system measured here represents a typical physical arrangement and, in general, a single set of values (with some associated uncertainty) may be used to represent the connection stiffness and damping for a particular holder. However, this has not been rigorously investigated at this time.

Once the connection coefficients were obtained, the analytic direct and cross FRFs for the tool and experimental holder/spindle direct FRF (note that *no modal fit is necessary*, experimental data is sufficient for the RCSA method) were then inserted in Eq. (15) and the tool point dynamic response predicted. Experimental impact tests were also performed for each of the three selected tools. A comparison of the results follows.

Figure 6 shows the experimental and predicted Y direction tool point FRFs (G_{11}) for length:diameter ratios of 8:1, 9:1, and 10:1. The overall agreement between the predicted and measured results is good. However, small deviations are also seen. This is attributed in part to variations in collet torque between the three tool setups (no special steps were taken to control collet torque), imperfect knowledge of tool length/geometry, deviations in contact conditions between the collet and tool, and finite repeatability of the FRF measurement process, which was determined to have standard uncertainties (denoted u) of 1 Hz, 6.8×10^4 N/m, and 4×10^{-4} for the measured natural frequency (f_n), stiffness (k), and damping ratio (ζ), respectively, by a Type A (statistical) evaluation of representative data [27].

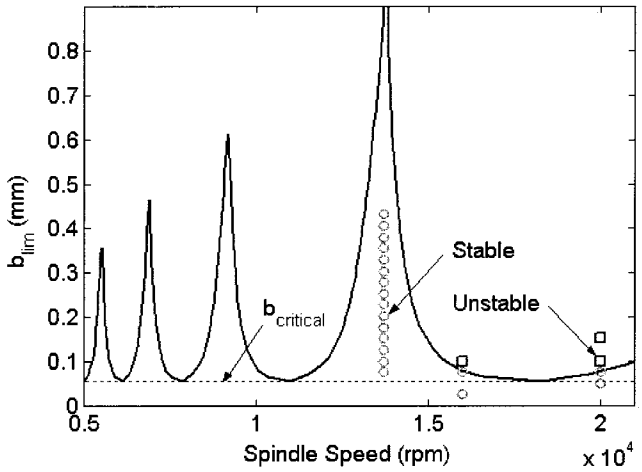

Fig. 7 Stability lobe diagram (9:1 tool)

The transition from the 8:1 to 9:1 case results in the anticipated decrease in both natural frequency and stiffness. For the 10:1 tool, however, the single tool mode seen in the 9:1 case has been effectively split into two dynamically stiffer modes, providing an increase in stability. This is due to interaction of the cantilever tool mode with the approximately 727 Hz Y direction holder/spindle mode (shown in Fig. 5). The analog to this situation is the dynamic absorber, where a small spring/mass is added to a larger vibrating system. The spring constant and mass of the added system are selected such that the natural frequency is equal to the excitation frequency of the larger structure and the vibration of the support structure is reduced, theoretically, to zero (for zero damping) at the driving frequency. Alternately, this effect may be described as proper impedance matching between the tool and holder/spindle substructures.

Figure 6 shows that interaction between tool and holder/spindle modes can dramatically affect the tool point FRF. To illustrate the effect of this interaction on machining performance, stability lobe diagrams for slotting cuts in the machine Y direction have been developed for the 9:1 and 10:1 tools [11]. These are shown in Figs. 7 and 8. Additionally, these figures include machining verification results superimposed on the analytic lobes, where stable cuts are represented by circles and unstable cuts by squares (chatter was verified by both visual inspection of the cut surface and the frequency content of the machining audio signal [6]). It is seen that the 10:1 cutter offers a significantly higher critical (or asymptotic) stability limit (maximum stable axial depth of cut at all spindle speeds) than the 9:1 cutter, as well as a shift in the location of the stability lobes. This implies two possible optimization parameters: (1) tool length selection for interaction with holder/spindle modes to increase the local stability limit, and (2) tool length selection to move a highly stable lobe to the top spindle speed of the machine (e.g., for a top spindle speed of 20,000 rpm, the 10:1 tool would be selected) [15].

To further investigate the interaction of tool modes with holder/spindle modes, RCSA simulations were completed for 7:1 (82.6 mm overhang) to 12:1 (141.6 mm overhang) tools to predict the

[2]Because the accurate identification of the connection parameters (between the tool and holder, in this case) defines the RCSA predictive capability, special steps may be required to assure dynamic repeatability. For example, initial studies have indicated a dependence of the tool point dynamic stiffness on the collet torque, which leads to the necessity of using a torque wrench (or other control apparatus) to set the collet torque. The dynamic repeatability of the system will therefore provide a lower bound on the predictive performance; in an analogous manner, the static positioning repeatability bounds the positioning accuracy of a machine tool.

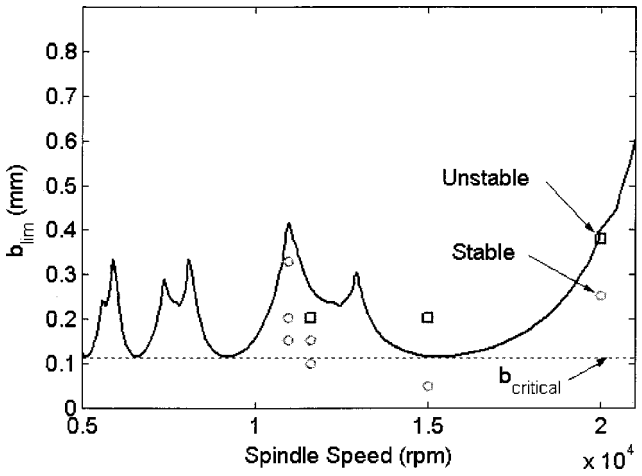

Fig. 8 Stability lobe diagram (10:1 tool)

tool point FRF and the corresponding stability lobes were constructed [11]. The absolute critical stability limit (b_{critical}) from the analytic stability lobe diagrams was then recorded for each tool overhang length. The predicted slotting critical stability limits are plotted versus tool length in Fig. 9. Increased stability is recognized at tool frequencies which correspond to holder/spindle modes (approximately 1114, 727, and 540.4 Hz). Although the expected general trend of decreasing stability for increasing tool length is seen, significant local increases in stability due to the "dynamic absorber effect" are also recognized. The improved stability offered by the 727 Hz mode interaction (10:1 tool) agrees with the machining test results shown in Fig. 8 and reported in [4].

4.2 19.1 mm Diameter Tooling. A receptance coupling analysis was also completed for a 19.1 mm diameter, 98.5 mm overhang tungsten carbide endmill secured in a shrink-fit, rather than collet type, HSK 63A holder. The analytic tool FRFs were derived and coupled to an experimental measurement of the holder/spindle combination in the X and Y coordinate directions. Similar to the previous case, a single experimental measurement of the assembly (in the X direction) was used to determine the connection parameters (shown in Table 2), then these parameters were used to predict the system response in the Y direction.

Figure 10 displays the predicted and measured tool point FRFs for the Y direction. Again, good qualitative agreement is seen with

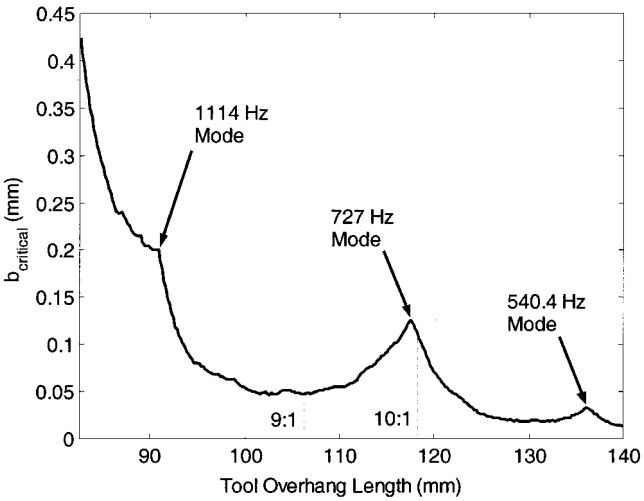

Fig. 9 Critical stability limits vs. tool length (11.8 mm diameter tooling)

Table 2 Stiffness/damping coefficients for 19.1 mm diameter, four flute tooling (identified from X direction measurement)

k_x (N/m)	k_θ (N-m/rad)	c_x(N-s/m)	c_θ (N-m-s/rad)
$4.8\text{x}10^7$	$3.2\text{x}10^6$	80	21

slight deviations due to uncertainties in the measurement procedure (the combined standard uncertainties listed in Section 4.1 are again applicable) and system geometry. It is also recognized that the stiffer tool allows greater participation of the spindle modes in the tool point response (and, correspondingly, a stronger chance for asymmetry in the X and Y direction FRFs), as opposed to the example in Section 4.1 where the final response was dominated by the rather flexible cantilever tool mode. In both cases, however, it is the *combined relationship of the tool and spindle modes* that defines the system response.

To further verify the receptance coupling method performance, direct and cross FRFs were measured on the tool/holder/spindle assembly at six axial locations (equally spaced points from the tool free end to holder face) in the Y direction and the dominant mode shape determined (with an approximate natural frequency of 1208 Hz). These experimental results are compared to mode shapes derived from RCSA predictions (i.e., G_{11}, G_{12}, G_{13}, G_{14}, G_{15}, and G_{16}) at the same spatial locations in Fig. 11.

The combined standard uncertainty of the measured results may be determined from the *law of propagation of uncertainty* [27]. Figure 11 was obtained by recording the minimum value of the imaginary part of the selected mode (1208 Hz) for each of the direct and cross FRFs. An estimate of this minimum value (for well-separated modes) may be obtained according to Eq. (21). The combined standard uncertainty, u_c, is then written as shown in Eq. (22) (zero covariance between modal stiffness and damping values has been assumed).

$$\min(\text{Im}[G(\omega)]) \cong \frac{1}{2k\zeta} \tag{21}$$

$$u_c^2 = \left(\frac{\partial f}{\partial k}u(k)\right)^2 + \left(\frac{\partial f}{\partial \zeta}u(\zeta)\right)^2 = \left(\frac{1}{2k\zeta}\right)^2\left(\frac{u^2(k)}{k^2} + \frac{u^2(\zeta)}{\zeta^2}\right) \tag{22}$$

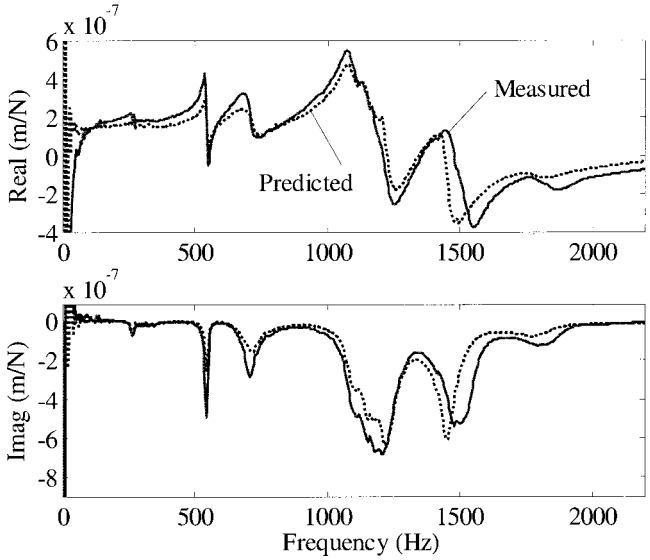

Fig. 10 Y direction tool point direct FRF (19.1 mm diameter tooling)

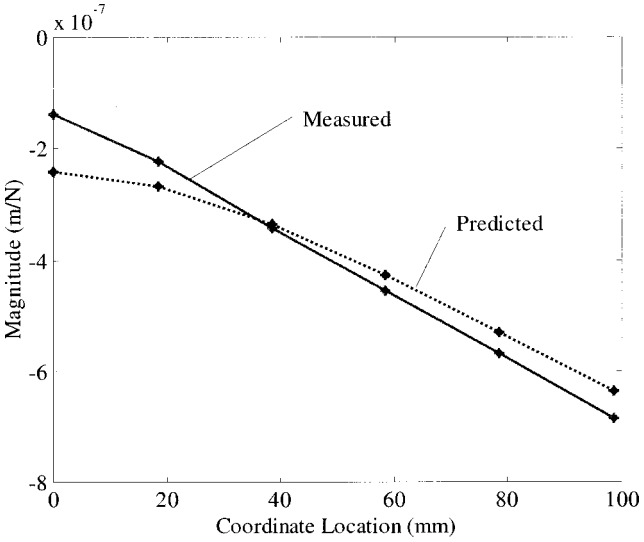

Fig. 11 Y direction mode shape comparison (19.1 mm diameter tooling)

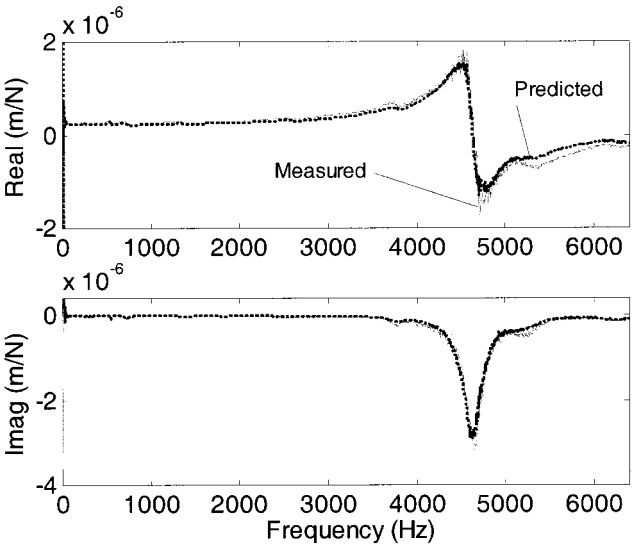

Fig. 13 Y direction tool point direct FRF (23.5 mm overhang)

Table 3 Stiffness/damping coefficients 6.35 mm diameter, four flute tooling (identified from 26 mm overhang configuration)

k_x (N/m)	k_θ (N-m/rad)	c_x(N-s/m)	c_θ (N-m-s/rad)
$1.7\text{x}10^7$	$2.9\text{x}10^5$	42	5.6

Substitution of the standard uncertainties for modal stiffness and damping ratio (given in Section 4.1) and representative stiffness and damping ratio values for the selected mode gives a combined standard uncertainty of 6.1×10^{-9} m/N.

4.3 6.35 mm Diameter Tooling. Finally, a *tool tuning* case study has been completed for a 6.35 mm diameter, 63.5 mm long, 4 flute, tungsten carbide endmill (collet HSK 63A holder). In this case, the minimum and maximum tool overhang lengths were determined to be 23.5 and 44.45 mm, respectively, from the tool geometry (i.e., flute length and minimum collet insertion length). An initial overhang of 26 mm (previously selected by the machinist) was used to determine the connection parameters (a single tool point measurement was performed in the machine X direction), then these values were used to select the tool length (within the preselected range) for maximized b_{critical} by RCSA simulation. Once the appropriate overhang was determined, a stability lobe diagram was then generated to select the best spindle speed for maximized MRR.

The connection parameters are summarized in Table 3. The variation in critical stability limit for slot machining aluminum in the X coordinate direction is shown in Fig. 12 (due to spindle and tool symmetries, the Y direction result is nearly identical and is not shown). Figure 12 demonstrates a special case; although the ''dynamic absorber effect'' causes local increases in the critical limit (with spindle modes of approximately 3840, 3220, and 2604 Hz), these improvements cannot overcome the stability reduction imposed by the increased tool length and the most favorable overhang (with respect to the critical stability limit) is the minimum allowed by the tool geometry (23.5 mm). A stability lobe analysis for this new tool length recommends an operating spindle speed of 17305 rpm (for a maximum available spindle speed of 20,000 rpm).

Impact testing was also performed to verify the RCSA results. Comparisons between the predicted and measured X and Y direction FRFs for the selected 23.5 mm overhang showed good qualitative agreement. The Y direction result is shown in Fig. 13; the X result is similar.

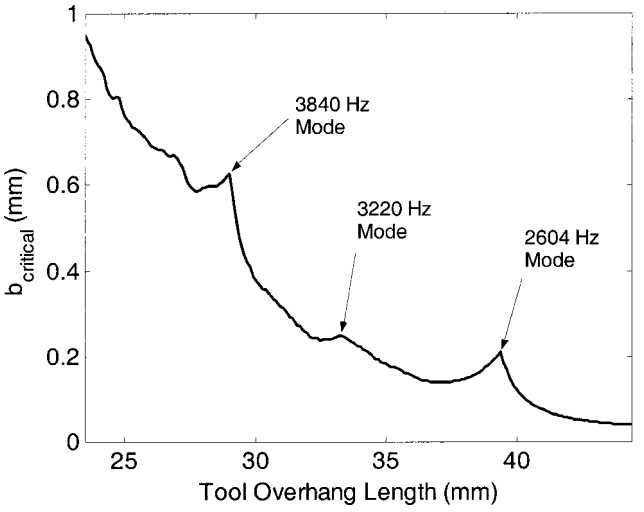

Fig. 12 Critical stability limit variation (6.35 mm diameter tooling)

5 Conclusions

The application of receptance coupling substructure analysis (RCSA) to tool point FRF prediction has been demonstrated. It was shown that analytic expressions for tool FRFs could be coupled with holder/spindle experimental FRFs to predict the assembly's dynamic response.

A *tool tuning* example, in which long, slender tools were coupled to a collet-type HSK 63A holder, provided initial verification of the method. Experimental and predicted results showed dramatic variations in the tool point response as tool modes interacted with holder/spindle modes, similar to the effect seen in dynamic absorbers. Predicted local increases in the critical stability limit matched empirical machining results. Stability lobe diagrams were also generated and it was shown that two optimization criteria for proper tool length may be selected: (1) maximize the critical stability limit, and (2) maximize the chatter free axial depth of cut at the top available spindle speed. Further experimental verification was provided by comparisons between measured

and predicted FRFs and mode shapes for shrink-fit tooling with higher dynamic stiffness and a *tool tuning* case study for rather flexible, 6.35 mm diameter tooling.

Acknowledgments

The authors gratefully acknowledge support from an NRC/NIST Postdoctoral Research Fellowship (for T. Schmitz). They would also like to thank Dr. Jon Pratt of NIST for helpful suggestions.

References

[1] Smith, S., Winfough, W., and Halley, J., 1998, ''The Effect of Tool Length on Stable Metal Removal Rate in High-Speed Milling,'' CIRP Ann., **47**, No. 1 pp. 307–310.
[2] Agapiou, J., Rivin, E., and Xie, C., 1995, ''Toolholder/Spindle Interfaces for CNC Machine Tools,'' CIRP Ann., **44/1**, pp. 383–387.
[3] Schultz, H., and Moriwaki, T., 1992, ''High-Speed Machining,'' CIRP Ann., **41**, No. 2 pp. 637–643.
[4] Davies, M., Dutterer, B., Pratt, J., and Schaut, A., 1998, ''On the Dynamics of High-Speed Milling with Long, Slender Endmills,'' CIRP Ann., **47**, No. 2, pp. 55–60.
[5] Weck, M., and Schubert, I., 1994, ''New Interface Machine/Tool: Hollow Shank,'' CIRP Ann., **43**, No. 1, pp. 345–348.
[6] Delio, T., Tlusty, J., and Smith, S., 1992, ''Use of Audio Signals for Chatter Detection and Control,'' ASME J. Eng. Ind., **114**, pp. 146–157.
[7] Smith, S., and Tlusty, J., 1991, ''An Overview of Modeling and Simulation of the Milling Process,'' ASME J. Eng. Ind., **113**, pp. 169–175.
[8] Tlusty, J., Zaton, W., and Ismail, F., 1983, ''Stability Lobes in Milling,'' CIRP Ann., **32**, No. 1, pp. 309–313.
[9] Altintas, Y., and Budak, E., 1995, ''Analytical Prediction of Stability Lobes in Milling,'' CIRP Ann., **44**, No. 1, pp. 357–362.
[10] Altintas, Y., and Lee, P., 1996, ''A General Mechanics and Dynamics Model for Helical End Mills,'' CIRP Ann., **45**, No. 1, pp. 59–64.
[11] Budak, E., and Altintas, Y., 1998, ''Analytical Prediction of Chatter Stability Conditions for Multi-Degree of Freedom Systems in Milling. Part I: Modeling, Part II: Applications,'' ASME J. Dyn. Syst., Meas., Control, **120**, pp. 22–36.
[12] Koenisberger, F., and Tlusty, J., 1967, *Machine Tool Structures-Vol. I: Stability Against Chatter*, Pergamon Press.
[13] Merrit, H., 1965, ''Theory of Self-Excited Machine Tool Chatter,'' ASME J. Eng. Ind., **87**, pp. 447–454.
[14] Minis, I., Yanushevsky, T., Tembo, R., and Hocken, R., 1990, ''Analysis of Linear and Nonlinear Chatter in Milling,'' CIRP Ann., **39**, pp. 459–462.
[15] Schmitz, T., and Donaldson, R., 2000, ''Predicting High-Speed Machining Dynamics by Substructure Analysis,'' CIRP Ann., **49**, No. 1, pp. 303–308.
[16] Tlusty, J., Smith, S., and Winfough, W., 1996, ''Techniques for the Use of Long Slender End Mills in High-Speed Machining,'' CIRP Ann., **45**, No. 1, pp. 393–396.
[17] Tlusty, J., and Ismail, F., 1980, ''Dynamic Structural Identification Tasks and Methods,'' CIRP Ann., **29**, No. 1, pp. 251–255.
[18] Tlusty, J., Smith, S., and Zamudio, C., 1991, ''Evaluation of Cutting Performance of Machining Centers,'' CIRP Ann., **40**, No. 1, pp. 405–410.
[19] Smith, S., Jacobs, T., and Halley, J., 1999, ''The Effect of Drawbar Force on Metal Removal Rate in Milling,'' CIRP Ann., **48**, No. 1, pp. 293–296.
[20] Ferreira, J., and Ewins, D., 1995, ''Nonlinear Receptance Coupling Approach Based on Describing Functions,'' *Proceedings of the 14th International Modal Analysis Conference*, Dearborn, MI, pp. 1034–1040.
[21] Ferreira, J., 1996, ''Transfer Report on Research Dynamic Response Analysis of Structures with Nonlinear Components,'' Internal Report-Dynamics Section, Imperial College, London, UK.
[22] Ren, Y., and Beards, C., 1993, ''A Generalized Receptance Coupling Technique,'' *Proceedings of the 11th International Modal Analysis Conference*, Kissimmee, FL, pp. 868–871.
[23] Klosterman, A., McClelland, W., and Sherlock, I., 1977, ''Dynamic Simulation of Complex Systems Utilizing Experimental and Analytical Techniques,'' ASME, 75-WA/Aero-9.
[24] Ewins, D., 1995, *Modal Testing: Theory and Practice*, Research Studies Press, Ltd., Somerset, England.
[25] Blevins, R., 1979, *Formulas for Natural Frequency and Mode Shape*, Van Nostrand Reinhold Co., New York, NY.
[26] Avitabile, P., 2000, ''Modal Space: Back to Basics,'' *Experimental Techniques*, **24**, No. 5, pp. 15–16.
[27] Taylor, B., and Kuyatt, C., 1994, ''Guidelines for Evaluating and Expressing the Uncertainty of NIST Measurement Results,'' NIST Technical Note 1297.